

MOLECULAR PHYSICS

Quantum state tracking and control of a single molecular ion in a thermal environment

Yu Liu^{1,2,*}, Julian Schmidt^{1,2}, Zhimin Liu^{1,2}, David R. Leibrandt^{1,2},
Dietrich Leibfried^{1,2}, Chin-wen Chou^{1,2}

Understanding molecular state evolution is central to many disciplines, including molecular dynamics, precision measurement, and molecule-based quantum technology. Details of this evolution are obscured when observing a statistical ensemble of molecules. Here, we report real-time observations of thermal radiation-driven transitions between individual states (“jumps”) of a single molecule. We reversed these jumps through microwave-driven transitions, which resulted in a 20-fold improvement in the time the molecule dwells in a chosen state. The measured transition rates showed anisotropy in the thermal environment, pointing to the possibility of using single molecules as *in situ* probes for the strengths of ambient fields. Our approaches for state detection and manipulation could apply to a wide range of species, facilitating their uses in fields including quantum science, molecular physics, and ion-neutral chemistry.

The ability to follow the evolution of molecules at the level of their quantum states has revolutionized how we study the dynamics that occur in these systems.

Resolving molecular states at progressively smaller energy scales often leads to the understanding of finer dynamical details. For example, resolving the vibrational states elucidates how energy flows within a molecule (1) and in chemical reactions (2); resolving the rotational states provides insights into the interaction potential that governs molecular scatterings (3, 4); and further resolving the spin-rotational states reveals the subtle role magnetic interactions play in intramolecular dynamics (5) and reactions (6). High-resolution state detection has proven especially imperative for observing quantum mechanical effects in molecular dynamics such as resonance (7, 8), interference (9), geometric phase (10), and entanglement (11, 12). Continued progress in the experimental resolution of molecular states will provide new opportunities for the study, and ultimately the control, of molecular dynamics.

Over the past few decades, advances in atomic, molecular, and optical physics have enabled the manipulation and detection of pure molecular states in trapped, translationally cold neutral molecules. High-fidelity detection of individual molecular states is primarily accomplished through the fluorescence or absorption of photons, either on the molecules

themselves (13) or on atoms that are dissociated from these molecules (14). These capabilities have instigated efforts toward the broad application of molecules in quantum science and technology, including precision measurement (15), quantum simulation (16, 17), and quantum computation (18, 19). The use of these highly refined techniques to study molecular dynamics, however, remains challenging owing to the need for repeated scattering of a large number of photons during detection (i.e., “photon-cycling”), which requires a suitable level structure. Furthermore, the large translational energy deposition that occurs in many molecular processes (e.g., reactions and collisions) causes Doppler broadening of transitions that render many states unresolvable.

State manipulation and detection techniques for molecular ions have developed alongside those for neutral molecules. In recent years, quantum logic spectroscopy (QLS), a technique originally developed for atomic ion optical clocks (20), has emerged as a new method for state preparation and measurement of single molecular ions (21–23). With QLS, the quantum state information can be mapped between a molecular ion and a cotrapped, laser-cooled atomic ion by means of their coupled motion within an ion trap. In this way, QLS allows for projective preparation of the molecular ion in a pure quantum state as well as non-destructive state readout, all while leveraging the photon-cycling ability of the atomic ion. The atomic ion further provides efficient sympathetic cooling of the translational motions of the molecular ion to near-ground states, even in cases of large energy deposition into the translational motions (24). Finally, both the translational cooling and QLS can be performed with few requirements on the molecular-level structure and are therefore applicable to a wide variety of internal states and species. Numerous planned and ongoing experiments

aim to leverage the precision and versatility of QLS for precision spectroscopy of a range of different species (25–28). These features make QLS-controlled molecular ions a promising platform to study molecular dynamics at the single-particle level and with full state resolution.

In this study, we developed a QLS-based protocol to track and control the state evolution of a single CaH^+ molecular ion under environmental perturbations in a room temperature ultrahigh vacuum apparatus. Possible sources of perturbation include thermal radiation (TR) and background gas collisions. We observed transitions (“quantum jumps”) between individual states of the molecule and found them consistent with being TR-driven. By applying microwave pulses to drive rotational transitions in real time conditioned on the detected state, we reversed undesired state changes and confined the molecule within a target state for periods of ~20 times its lifetime without such control. The improved control over the state of the molecule increased the duty cycle with which operations such as spectroscopic transitions and quantum gates may be carried out from ~7% to ~65%. Measurements of transition rates between different molecular states suggested that the environment deviated from an ideal blackbody, demonstrating the potential of the molecule as a highly localized quantum sensor for its environment.

Quantum logic detection of quantum jumps in CaH^+

Our experimental setup is schematically shown in Fig. 1A and described in detail elsewhere (22). In brief, an ion crystal consisting of a $^{40}\text{Ca}^+$ and a $^{40}\text{CaH}^+$ is confined in a linear radio frequency (RF) trap at room temperature and under ultrahigh vacuum ($\leq 10^{-8}$ Pa). Several coupled modes of the translational motion of the ions are cooled to the ground state through a combination of Doppler cooling, electromagnetically induced transparency cooling, and resolved sideband cooling. All cooling steps leverage precise control over the internal states of Ca^+ and do not involve those of CaH^+ . Internal degrees of freedom of CaH^+ may thermalize to the environment (29) through interaction with the TR emitted by surrounding surfaces or through collisions with residual background gas molecules (predominantly H_2). These interactions result in a distribution in the probability of finding the molecule in various rotational manifolds, labeled by the quantum number J (Fig. 1A, inset). Within a given J -manifold, the probability is further divided evenly among $4J + 2$ spin-rotational sublevels $|\mathcal{J}\rangle \equiv |J, m, \xi\rangle$, where m is the sum of the quantum numbers for the nuclear spin and rotational angular momentum projections (m_l and m_s) along the quantization axis defined

¹Time and Frequency Division, National Institute of Standards and Technology, Boulder, CO 80305, USA. ²Department of Physics, University of Colorado, Boulder, CO 80309, USA.

*Corresponding author. Email: yuliu@umd.edu

†Present address: Department of Chemistry and Biochemistry, University of Maryland, College Park, MD 20742, USA.

‡Present address: Paul Scherrer Institute (PSI), 5232 Villigen, Switzerland.

§Present address: Department of Physics and Astronomy, University of California, Los Angeles, CA 90095, USA.

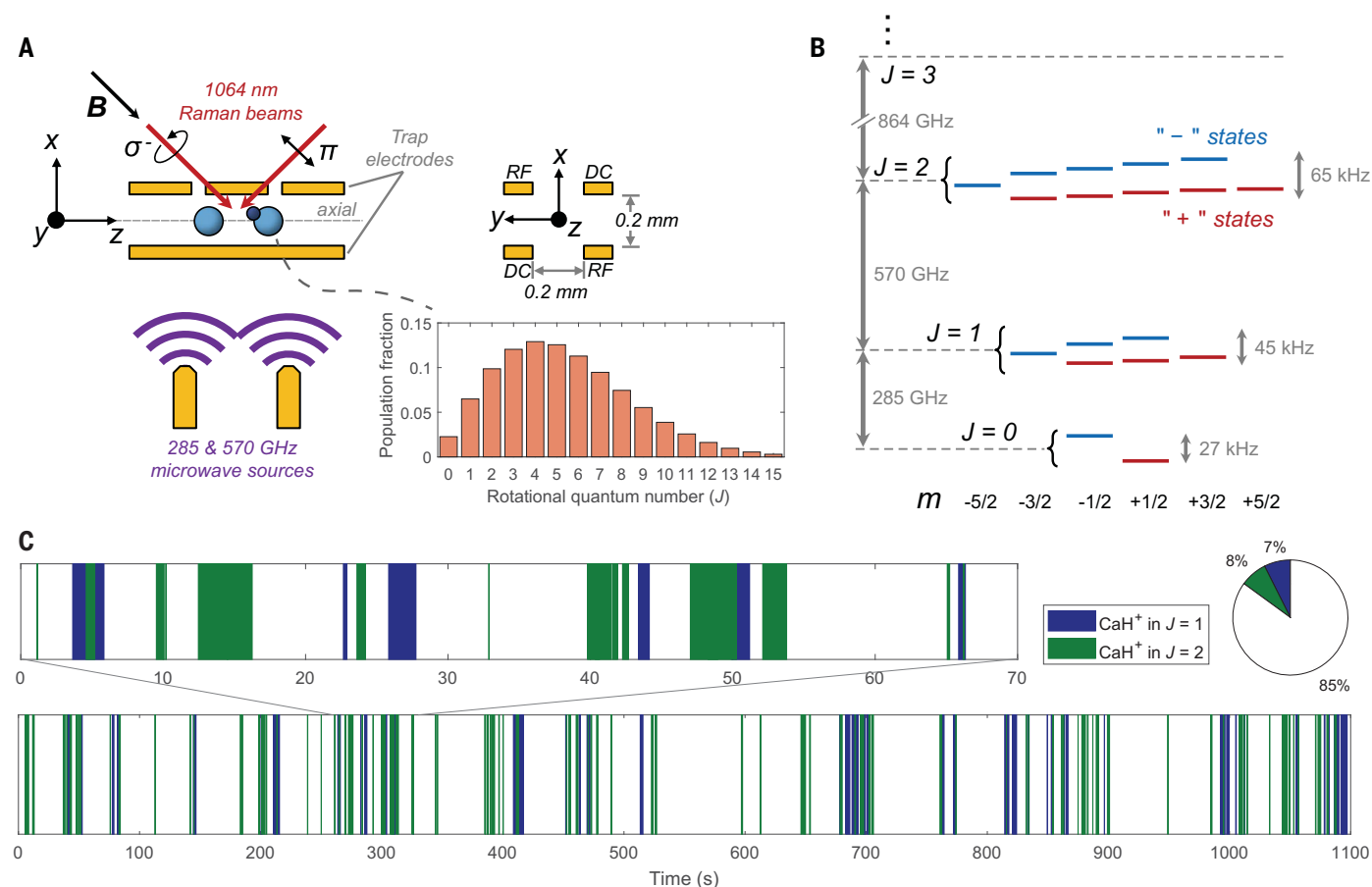


Fig. 1. Experimental setup and rotational dynamics in CaH^+ . (A) Schematic of the setup for QLS operation on CaH^+ . A single $^{40}\text{Ca}^+$ and single $^{40}\text{CaH}^+$ are cotrapped in a linear RF trap and form a Coulomb crystal along the axial (z) direction. A magnetic quantization field of 6.5 G was directed diagonally in the xz plane. Molecular transitions within each J -manifold were driven by a pair of 1064-nm laser beams in Raman configuration (red arrows), and those between different J -manifolds were driven by microwave radiations at hundreds of gigahertz (purple). A view of the trap along the axial direction shows the arrangement of the direct current (DC) and RF electrodes. (Inset) The probability of finding the

molecule in various rotational manifolds in the vibrational and electronic ground state of CaH^+ , according to a 300 K Boltzmann distribution. (B) Energy level structure of CaH^+ for the first few rotational manifolds in the vibrational and electronic ground state (not to scale) in the presence of a 6.5-G magnetic field (B) and a co-aligned 1300 V/m residual trap RF electric field (SM). Blue (red) lines represent states with $\xi = - (+)$. (C) Real-time observation of molecular state changes between $J = 1$ (blue), $J = 2$ (green), and J other than 1 or 2 (white). (Top left panel) A zoomed-in view over a particular time period to show details. (Top right panel) A pie chart showing the fractional time the molecule is found in each manifold.

by a laboratory magnetic field (B in Fig. 1A), and $\xi \in \{+, -\}$ indicates the relative sign in the superposition of product states with the same m but opposite nuclear spin, that is, $|J, m, \pm\rangle \equiv c^-|J, m_J = m + 1/2\rangle|m_I = -1/2\rangle \pm c^+|J, m_J = m - 1/2\rangle|m_I = +1/2\rangle$, with $c^-, c^+ > 0$. For the extreme sublevels $|J, m = \pm(J + 1/2), \pm\rangle = |J, m_J = \pm J\rangle|m_I = \pm 1/2\rangle$, which are simple product states, ξ indicates the sign of m (22). Figure 1B shows the spin-rotational level structure of CaH^+ in its vibrational and electronic ground state ($v = 0, X^1\Sigma$) in the presence of external fields applied during experiments described in this work (see figure caption). One may also view the thermal distribution in a time-dependent picture, in which the molecular state evolves under the influences of external perturbations, causing the observed state to change sporadically (i.e., quantum jumps). State changes driven by TR follow dipole selec-

tion rules $\Delta J = \pm 1$ and $\Delta m = 0, \pm 1$, and those driven by collisions can take a wide range of ΔJ and Δm values.

We used QLS to nondestructively observe the molecular state and track its evolution under external influences. All QLS operations involved a pair of 1064-nm laser beams, which drove, in a far-off-resonance Raman configuration, transitions between neighboring sublevels within a J -manifold. To detect whether the molecule was in J , we first concentrated the probability of finding the molecule distributed among the $4J + 2$ sublevels into the extreme sublevel $|J, m = -J - 1/2, -\rangle$ through pumping and then attempted a projection by means of the transition $|J, m = -J - 1/2, -\rangle \rightarrow |J, m = -J + 1/2, -\rangle$ [see supplementary materials (SM) and (22)]. Following an initial successful projection, the molecule could be repeatedly reprojected in J until a quantum jump occurred,

and coherent operations such as spectroscopy (22, 30, 31) or entanglement (32) could be performed on a known, pure initial molecular state between reprojections. Figure 1C shows real-time observation of the molecule undergoing quantum jumps in and out of $J = 1$ and 2 in an experimental sequence where we made repeated and alternating detection attempts in these two manifolds. Each time the molecule was projected into $J = 1$ ($J = 2$), it spent, on average, 1.5(2) [0.7(1)] s before leaving [throughout the article, we use one standard deviation (1 SD) error as the measurement uncertainty]. The fractional time the molecule spent in each manifold defines the maximum duty cycle, D , over which we can perform coherent manipulations. Over the sequence in Fig. 1C, we measured $D \sim 7\%$ for $J = 1$ and 8% for $J = 2$. In this work, we did not attempt detection in $J \geq 3$, which collectively contained $\sim 80\%$ of

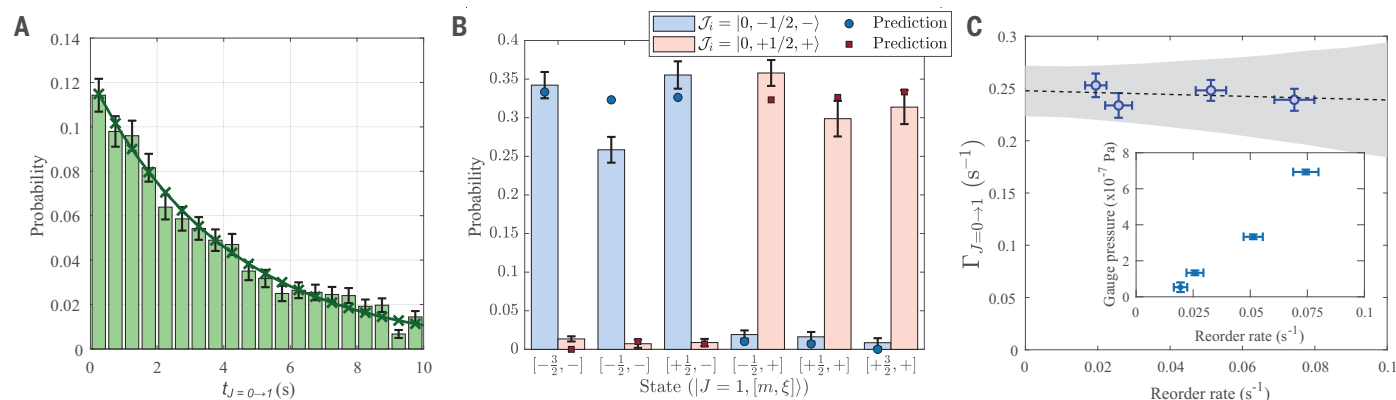


Fig. 2. Sublevel resolved quantum state jumps from $J = 0$ to 1 . (A) Normalized histogram of durations between the molecule's initialization in $|0, -1/2, -\rangle$ and its projection into any $|\mathcal{J} \in J = 1\rangle$ sorted into 0.5-s time bins (light-green bars). The data were obtained using the pump & project method. The histogram was fitted to an exponential decay, yielding a rate constant of $\Gamma_{J=0 \rightarrow 1} = 0.244(8) \text{ s}^{-1}$. (B) Normalized histograms of observed jumps from either $|0, -1/2, -\rangle$ (light-blue bars) or $|0, +1/2, +\rangle$ (light-red bars) to each sublevel $|\mathcal{J} \in J = 1\rangle$, and corresponding probabilities calculated assuming that the jumps conserved the nuclear spin of CaH^+ (dark-blue dots and dark-red squares). The data were obtained using the

state-resolved method. (C) Total rate for $J = 0 \rightarrow 1$ jumps, measured by the pump & project method, for different reorder rates of the Ca^+ - CaH^+ ion crystal. The data points (blue circles) were fitted to a linear function (black dashed line), yielding a slope of $-0.09(0.25)$ and a vertical offset of $0.248(12) \text{ s}^{-1}$, consistent with no significant rate change due to background gas collisions in this pressure range. The light-gray patch represents the 1 SD confidence interval for the fit, obtained through parametric bootstrapping. (Inset) Dependence of the ion reorder rate on the reading of a pressure gauge in the same vacuum system as the ion trap. All error bars in this figure represent 1 SD uncertainty.

the probability in a 300 K Boltzmann distribution (Fig. 1A, inset), owing to current limitations on the pumping efficiency for manifolds with large numbers of sublevels (SM).

Mechanism behind the observed jumps

To improve control over the molecular state and increase the duty cycle of our experiments, we first had to develop an understanding of the mechanisms driving the dynamics in our system. To this end, we monitored quantum jumps within the state space $J \in \{0, 1\}$, which is the minimal subspace within which effects of TR and collisions may be observed. We began each experiment by initializing CaH^+ in one of two sublevels in $J = 0$, $|\mathcal{J}_i\rangle = |0, -1/2, -\rangle$ or $|0, +1/2, +\rangle$. In anticipation of the molecule jumping to $J = 1$, we then performed detection in this manifold using one of two methods (SM): (i) sequentially attempting QLS projection from each of the six sublevels in $J = 1$ (referred to as the “state-resolved” method); and (ii) pumping the six sublevels toward and attempting QLS projection from the extreme state $|1, -3/2, -\rangle$ (referred to as the “pump & project” method). The attempts were repeated until a successful projection, after which the molecule was re-initialized to $|\mathcal{J}_i\rangle$ for another iteration. The results were collected over many iterations and are summarized in Fig. 2.

Figure 2A shows the normalized histogram of durations between the molecule's initialization in $|0, -1/2, -\rangle$ and its projection into any $|\mathcal{J} \in J = 1\rangle$, which we refer to as $t_{J=0 \rightarrow 1}$. The distribution is well described by an exponential function ($e^{-\Gamma_{J=0 \rightarrow 1} t_{J=0 \rightarrow 1}}$) with a fitted rate constant of $\Gamma_{J=0 \rightarrow 1} = 0.244(8) \text{ s}^{-1}$, indicat-

ing that the observed jumps were a stochastic process with a mean rate of $\Gamma_{J=0 \rightarrow 1}$. Alternatively, we obtained $\Gamma_{J=0 \rightarrow 1}$ by dividing the number of observed jumps by the total sequence duration over which the data in Fig. 2A were collected and found its value to be $0.246(6) \text{ s}^{-1}$, consistent with the rate determined by the exponential fit. Figure 2B displays the probabilities of detecting the molecule in $|\mathcal{J} \in J = 1\rangle$ following its initialization in one of the two $|\mathcal{J} \in J = 0\rangle$ states. Comparing the two sets of data, we observe that a molecule initially prepared in $|0, -1/2\rangle$ ($|0, +1/2\rangle$) was predominantly found in the states with $\xi = -$ ($+$). At our operating magnetic field of 6.5 G, the spin and rotational angular momenta were reasonably decoupled, such that each sublevel had a dominant nuclear spin projection component (SM). In particular, the “-” (“+”) states had large amplitudes in the $m_I = -1/2$ ($+1/2$) component. As such, our observation suggested that the nuclear spin of the molecule was mostly preserved by the process causing the $J = 0 \rightarrow 1$ transitions. We compared the measured probabilities against those calculated assuming that the environment process coupled the rotational angular momenta ($|J, m_J\rangle$) but not the nuclear spins ($|I, m_I\rangle$) of the sublevels (SM) and found good overall agreement.

The observed nuclear spin conservation was consistent with the effects of TR, which drives electric dipole transitions. Most inelastic collisions tend to leave nuclear spins unchanged as well. To investigate the relative contributions of these two mechanisms to the observed jumps, we measured the rate of jumps at dif-

ferent background pressures. For each pressure value, we determined the rate at which the Ca^+ and CaH^+ exchanged their positions in the crystal owing to collisions, and we used this “reorder” rate as an in situ, relative measure of the total collision rate between the CaH^+ and background gas molecules (33). The reorder rate was well correlated to the reading of a nearby pressure gauge (Fig. 2C, inset). The results (Fig. 2C) showed no significant change in $\Gamma_{J=0 \rightarrow 1}$ over a factor of ~ 4 variation in the reorder rate. A linear fit to the data bounded the contribution of collisions to $\Gamma_{J=0 \rightarrow 1}$ to below 0.02 s^{-1} at our nominal operating pressure of $\lesssim 10^{-8} \text{ Pa}$. We did not experimentally investigate the effect of pressure on the rates of quantum jumps between other pairs of rotational manifolds. However, it is generally observed for diatomic molecules that probability for state-changing collisions tends to decrease for increasing initial rotational quantum number (J_i) or increasing difference to the final rotational quantum number ($\Delta J = J_f - J_i$) (34, 35). As such, collisions with background gas molecules are, in general, unlikely to be a major cause of J -changing transitions in CaH^+ over the range of conditions explored here. All subsequent experiments described here were carried out at or below a reorder rate of 0.02 s^{-1} .

Molecular state tracking and control

Having established TR as predominantly responsible for the observed quantum jumps between different J -manifolds, we designed a protocol to undo these changes and keep the molecular state within a target manifold J_i .

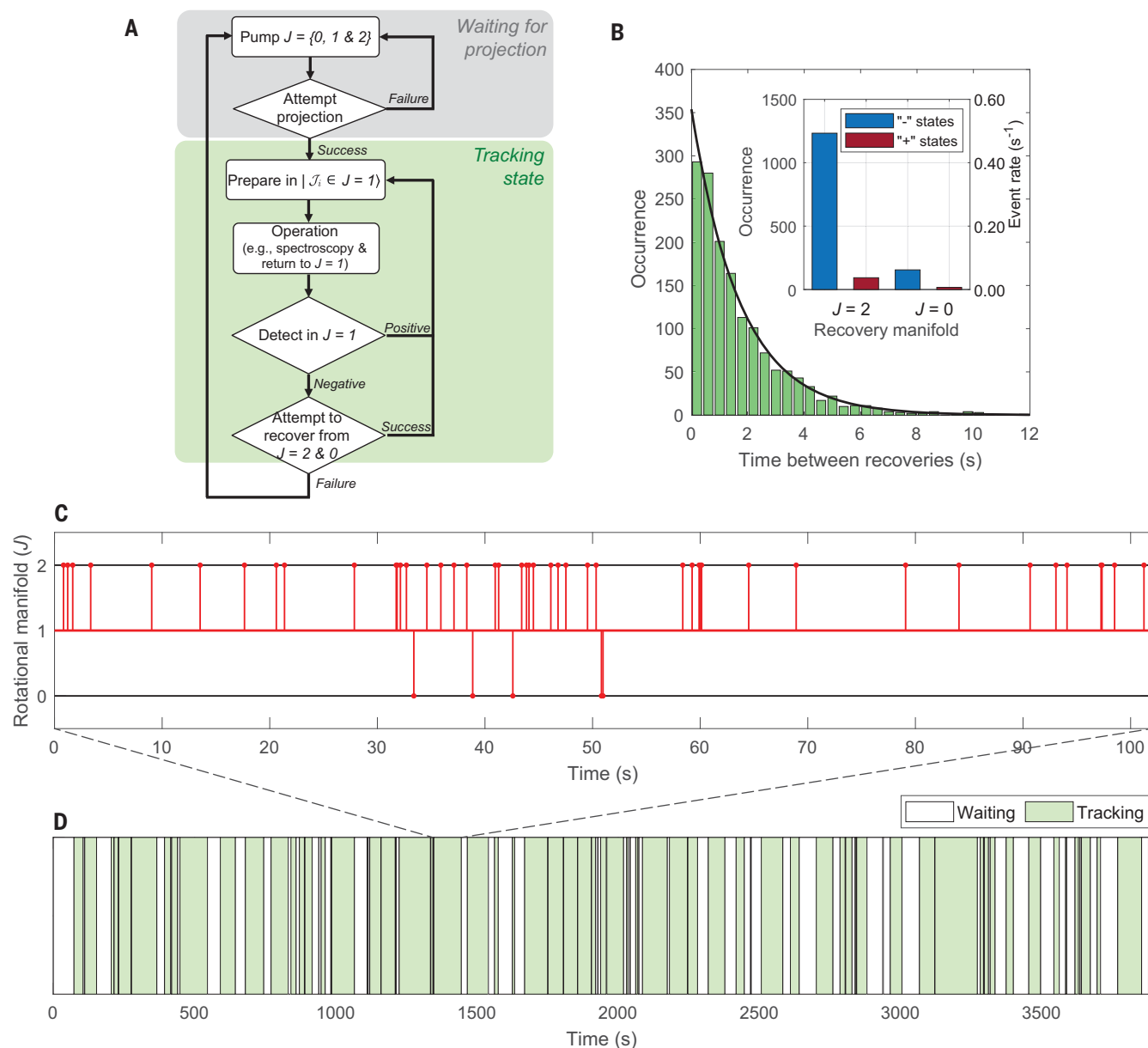


Fig. 3. Tracking and controlling the molecular state. (A) Flowchart for molecular state control. (B) Distribution of the time the molecule spent in $J = 1$ between two successive recoveries from $J = 0$ or 2 (green bars). A fit of the distribution to an exponential decay (black curve) yielded a $1/e$ time constant of $\tau_{J=1} = 1.71(6)$ s. (Inset) Number (left y axis) and rate (right y axis) of recovery events associated with the "+" and "-" states of $J = 0$ and 2 . Because the molecule was prepared in $|\mathcal{J}_i\rangle = |1, -1/2, -\rangle$, it was driven by TR predominantly to other "-" states.

(C) Real-time observation of quantum jumps from $J = 1$ to $J = 0$ and 2 . The molecular state at any point in time is indicated in red. Each vertical line marks a recovery event, which contained both the jump out of and recovery back to $J = 1$. Because the average time for a recovery was on order of 10 ms (SM), the two processes were not resolvable on the timescale of this plot. (D) Evolution of the molecule between the tracked ($J \in \{0, 1, 2\}$) and untracked ($J > 2$) subspaces during the execution of the protocol, marked by light-green and white patches, respectively.

Leveraging the $\Delta J = \pm 1$ selection rule that TR-driven transitions obey, we tracked quantum jumps from $J_i = 1$ to $J = 0$ and 2 and reversed them using electric dipole transitions driven by microwave π -pulses. The experiment began with repeated detection attempts in $J \in \{0, 1, 2\}$, during which we waited for TR to drive the molecule into this state space. Following a positive projection, we transferred the molecule to a certain sublevel $|\mathcal{J}_i \in J = 1\rangle$ and

began performing the desired operation, which generally entailed some coherent manipulation of the molecular state. In the event that the operation took the molecule out of $J = 1$ (e.g., spectroscopic probe of an excited rovibrational level), we returned the state to $J = 1$ afterward. We then detected whether the molecule still resided in $J = 1$ and, if so, transferred the state back to $|\mathcal{J}_i\rangle$ for another iteration of the operation. Failure to detect in $J = 1$ triggered a

recovery attempt that searched the neighboring manifolds $J = 0$ and 2 . The search began in $J = 2$, which represented an effective "border" of the state space we were working in, above which our state detection became less efficient (SM). If the molecule was detected in $J = 2$, we drove it back to $J = 1$ using a ~ 570 GHz microwave π -pulse; otherwise, we detected the two sublevels of $J = 0$ by coherently transferring any state amplitude in $|0, -1/2, -\rangle$ ($|0, 1/2, +\rangle$) to

$|1, -3/2, -\rangle$ ($|1, -1/2, -\rangle$) with a ~ 285 GHz microwave π -pulse and then attempting a projection. A direct QLS detection in $J = 0$ is currently not feasible because its two sublevels are not coupled by the 1064-nm Raman beams used for QLS operations (SM). If the molecule was successfully recovered back to $J = 1$, the experiment resumed; otherwise, tracking of the state was unsuccessful, and we had to wait for the molecule to reenter $J \in \{0, 1, 2\}$ after a period of uncontrolled evolution. A flowchart for the protocol is provided in Fig. 3A, and a timing diagram is provided in fig. S3.

To evaluate the effectiveness of this state control protocol, we executed it continuously for a duration of ~ 1 hour. For the purpose of this evaluation, the operation on the molecule was simply a 25-ms wait, and the molecule was in the state $|J_i\rangle = |1, -1/2, -\rangle$. The results are summarized in Fig. 3. Figure 3C shows TR-induced quantum jumps from $J = 1$ to $J = 0$ and 2 observed during a particular tracking period, which began with an initial preparation in $J = 1$ and ended with the failure to recover from $J = 0$ and 2. Figure 3B shows a histogram for the duration the molecule spends in $J = 1$ before jumping to a neighboring manifold. Fitting the histogram to an exponential decay, we found the lifetime of $J = 1$ to be $\tau_{J=1} = 1.71(6)$ s. The inset displays the number of times the molecule was recovered from $J = 0$ and 2 (left y axis). The results were separately tallied for the “+” and “−” states of each manifold. Dividing the number of recovery events by the total time the molecule spent in $J = 1$, we obtained the rates of the TR-induced transition from $J = 1$ to the neighboring manifolds (right y axis). Over the execution of the protocol, the system alternated between waiting for an initial projection and tracking the state (Fig. 3D). The average waiting period was $\bar{T}_{\text{wait}} = 19.3$ s, and the average tracking period was $\bar{T}_{\text{track}} = 35.5$ s. Thus, we found the duty cycle, defined as the fraction of time over which we could confine the molecule to $J = 1$, to be $D = \bar{T}_{\text{track}} / (\bar{T}_{\text{track}} + \bar{T}_{\text{wait}}) = 64.7\%$. This result represented an improvement of about one order of magnitude compared with when the state was not actively controlled (Fig. 1C). Mechanisms that limited the performance of our protocol are discussed in the SM.

Characterizing the thermal radiation environment with the molecule

For the discussions that follow, we emphasize the distinction between the terms “thermal radiation” (TR) and “blackbody radiation” (BBR). Throughout this article, TR refers to the electromagnetic radiation emitted as a result of the stochastic motion of particles in materials. TR that is emitted by an ideal blackbody, and therefore follow Planck’s law,

is referred to specifically as BBR. The spectrum of TR from realistic sources can differ from that of BBR owing to scattering or boundary conditions.

In many experiments, including trapped ion optical atomic clocks (36, 37), the interaction between particles and TR is a concern. During the tracking experiments summarized in Figs. 2 and 3, we obtained rates for TR-driven transitions between J -manifolds or even individual spin-rotational sublevels. These rates provided a local probe of the radiation environment in which the molecular ion was situated. The rate of TR-driven transition between a given pair of spin-rotational levels can be expressed as $\Gamma_{J,J'} = \rho_{\text{TR}} B_{J,J'} + A_{J,J'}$. Here, ρ_{TR} is the energy density of TR, A is the Einstein coefficient for spontaneous emission, and B is the Einstein coefficient for absorption or stimulated emission (SM). In an ideal blackbody environment, the radiation is randomly polarized, and its energy density is given by Planck’s law $\rho_{\text{BBR}}(\nu, T) = \frac{8\pi h \nu^3}{c^3} \frac{1}{\exp(h\nu/(k_B T)) - 1}$. Here, ν is the frequency of the radiation, and T is the temperature of the environment. Under the assumption that $\rho_{\text{TR}} = \rho_{\text{BBR}}$, we derived a value for T from $\Gamma_{J=0 \rightarrow 1}^{\text{meas.}} / (\Gamma_{J=1 \rightarrow 2}^{\text{meas.}})$, which is the

measured rate of transition between a sublevel in $J = 0$ ($J = 1$) and all allowed sublevels in $J = 1$ ($J = 2$) (Fig. 4A, top panel) (SM). The individual transitions that contributed to these total measured rates are highlighted in the bottom panel of Fig. 4A. Given the finite duration required for a molecular state detection, a certain fraction of transition events was not registered, making the measured rates an underestimate of the actual rates. As such, the derived T should be considered a lower bound. Nevertheless, we found even the lower estimates of T (400 and 333 K) to be higher than the ambient temperature of our experiment, which was ~ 300 K. Further details about the environment can be obtained by examining transitions between individual sublevels. In particular, we studied the degree to which the 285-GHz frequency component of TR was anisotropic by comparing the rates or probabilities of transitions between sublevels of $J = 0$ and 1 that were driven by different polarizations. Figure 4B shows the ratios between the energy densities of σ^- - and π -polarized TR, derived from the measured rates of three pairs of transitions highlighted in the inset (SM). The arrows indicate the direction of

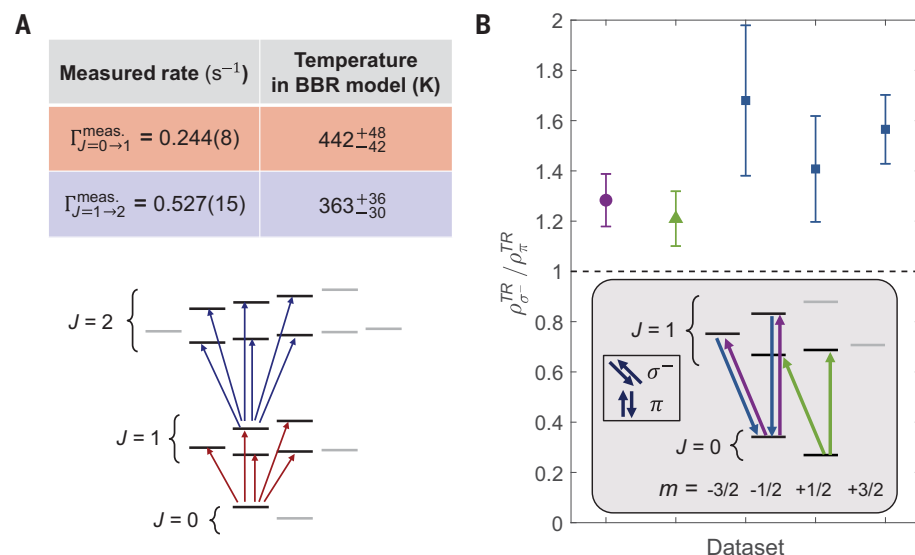


Fig. 4. Deviations from a blackbody environment. (A) (Top panel) Measured rates for $J = 0 \rightarrow 1$ jumps and $J = 1 \rightarrow 2$ transitions and the corresponding temperatures of a blackbody environment (T). Uncertainties in T were derived from the uncertainties of both $\Gamma^{\text{meas.}}$ and the permanent dipole moment of CaH^+ [5.34 ± 0.19 D (31)]. Because the measured rates underestimated the actual transition rates, the values for T should be considered as lower bounds. (Bottom panel) Individual transitions that contributed to $\Gamma_{J=0 \rightarrow 1}^{\text{meas.}}$ ($\Gamma_{J=1 \rightarrow 2}^{\text{meas.}}$), marked by red (blue) arrows. **(B)** Ratios between the energy densities of σ^- - and π -polarization components of TR ($\rho_{\sigma^-}^{\text{TR}}$ and ρ_{π}^{TR}) at around 285 GHz, derived from measurements on the three pairs of transitions indicated in the inset. The purple dot and green triangle points derive from the $J = 0 \rightarrow 1$ transition probabilities presented in Fig. 2B. The blue square points derive from the rates of $J = 1 \rightarrow 0$ transitions obtained during the tracking experiment summarized in Fig. 3, with the 25-ms wait applied and the molecule was in $|1, -3/2, -\rangle$ or $|1, -1/2, -\rangle$. The rate data for the blue square points were collected over three sets on different days. Error bars represent 1 SD uncertainty.

the transition. We observe that the ratios, which were derived from different measurements, were reasonably consistent with each other but larger than unity. Such a result was inconsistent with a randomly polarized field environment where the energy density for every polarization component is equal. Together, the data from Fig. 4, A and B, implied that the thermal environment in the hundreds of gigahertz spectral region deviated from an ideal blackbody at room temperature. Possible explanations of this deviation include the elevated temperatures of the electrodes due to the trap RF drive and the structure of our ion trap. On the latter point, the trap electrodes might be approximated as a set of conductive planes surrounding the molecular ion (Fig. 1A). Because the radiation components driving rotational transitions (285 and 570 GHz) have wavelengths (1.1 and 0.53 mm) that are longer than the spacing between these conductive planes (0.2 mm), their spectral and polarization characteristics might be substantially modified. Modification of the BBR spectrum by a cavity was observed in a previous work, in which sodium Rydberg atoms placed between two parallel plates experienced inhibited absorption of TR (38). Our results open the possibility of using a molecular ion as an in situ probe of its radiation environment (SM).

The molecular state control protocol demonstrated here is, in principle, generally applicable to heteronuclear molecular ions, which are susceptible to TR-driven dynamics (SM). Many proposed precision measurement experiments based on the platform of QLS on single molecular ions (25, 26, 28) aim to reach higher spectroscopic accuracy than the current records set by experiments using ensembles of ions (39–41). For these proposed experiments, improvements in state control would lead to a higher data rate and therefore reduced averaging time for spectroscopy. More broadly, we have demonstrated QLS as a ver-

satile and fully state-resolving tool for single-molecule state analysis. When combined with other well-established physical chemistry techniques such as ultrafast lasers and molecular beams that initiate the dynamics, QLS provides an opportunity to detect molecular response to external perturbations including strong-pulse excitation (42, 43) and inelastic collisions (44, 45) on an unprecedented single-molecule, single-state level.

REFERENCES AND NOTES

1. D. J. Nesbitt, R. W. Field, *J. Phys. Chem.* **100**, 12735–12756 (1996).
2. X. Yang, *Annu. Rev. Phys. Chem.* **58**, 433–459 (2007).
3. J. Andres, U. Buck, F. Huisken, J. Schleusener, F. Torello, *J. Chem. Phys.* **73**, 5620–5630 (1980).
4. J. M. Hutson, *Annu. Rev. Phys. Chem.* **41**, 123–154 (1990).
5. A. A. Milner, A. Korobenko, V. Milner, *New J. Phys.* **16**, 093038 (2014).
6. M.-G. Hu *et al.*, *Nat. Chem.* **13**, 435–440 (2021).
7. B. Margulis *et al.*, *Science* **380**, 77–81 (2023).
8. J. B. Kim *et al.*, *Science* **349**, 510–513 (2015).
9. W. Chen *et al.*, *Science* **371**, 936–940 (2021).
10. D. Yuan *et al.*, *Science* **362**, 1289–1293 (2018).
11. J. Li, S. Kais, *Sci. Adv.* **5**, eaax5283 (2019).
12. Y.-X. Liu *et al.*, *Science* **384**, 1117–1121 (2024).
13. E. S. Shuman, J. F. Barry, D. Demille, *Nature* **467**, 820–823 (2010).
14. K.-K. Ni *et al.*, *Science* **322**, 231–235 (2008).
15. ACME Collaboration, *Nature* **562**, 355–360 (2018).
16. L. Christakis *et al.*, *Nature* **614**, 64–69 (2023).
17. J.-R. Li *et al.*, *Nature* **614**, 70–74 (2023).
18. C. M. Holland, Y. Lu, L. W. Cheuk, *Science* **382**, 1143–1147 (2023).
19. Y. Bao *et al.*, *Science* **382**, 1138–1143 (2023).
20. P. O. Schmidt *et al.*, *Science* **309**, 749–752 (2005).
21. F. Wolf *et al.*, *Nature* **530**, 457–460 (2016).
22. C. W. Chou *et al.*, *Nature* **545**, 203–207 (2017).
23. M. Sinhal, Z. Meir, K. Najafian, G. Hegi, S. Willitsch, *Science* **367**, 1213–1218 (2020).
24. H. Hirzler *et al.*, *Phys. Rev. Lett.* **128**, 103401 (2022).
25. C. Wellers, M. R. Schenkel, G. S. Giri, K. R. Brown, S. Schiller, *Mol. Phys.* **120**, e2001599 (2022).
26. Y. Zhou, J. O. Island, M. Grau, *Phys. Rev. A* **109**, 033107 (2024).
27. K. Najafian, Z. Meir, S. Willitsch, *Phys. Chem. Chem. Phys.* **22**, 23083–23098 (2020).
28. G. Arrowsmith-Kron *et al.*, *Rep. Prog. Phys.* **87**, ad1e39 (2024).
29. A. Bertelsen, S. Jørgensen, M. Drewsen, *J. Phys. B At. Mol. Opt. Phys.* **39**, L83–L89 (2006).
30. C. W. Chou *et al.*, *Science* **367**, 1458–1461 (2020).
31. A. L. Collopy, J. Schmidt, D. Leibfried, D. R. Leibbrandt, C.-W. Chou, *Phys. Rev. Lett.* **130**, 223201 (2023).
32. Y. Lin, D. R. Leibbrandt, D. Leibfried, C. W. Chou, *Nature* **581**, 273–277 (2020).

33. A. M. Hankin *et al.*, *Phys. Rev. A* **100**, 033419 (2019).
34. T. A. Brunner, N. Smith, A. W. Karp, D. E. Pritchard, *J. Chem. Phys.* **74**, 3324–3341 (1981).
35. D. A. Kliner, R. L. Farrow, *J. Chem. Phys.* **110**, 412–422 (1999).
36. N. Huntemann, C. Sanner, B. Lipphardt, C. Tamm, E. Peik, *Phys. Rev. Lett.* **116**, 063001 (2016).
37. S. M. Brewer *et al.*, *Phys. Rev. Lett.* **123**, 033201 (2019).
38. A. G. Vaidyanathan, W. P. Spencer, D. Kleppner, *Phys. Rev. Lett.* **47**, 1592–1595 (1981).
39. S. Patra *et al.*, *Science* **369**, 1238–1241 (2020).
40. S. Alighanbari, G. S. Giri, F. L. Constantin, V. I. Korobov, S. Schiller, *Nature* **581**, 152–158 (2020).
41. T. S. Roussy *et al.*, *Science* **381**, 46–50 (2023).
42. K. Ohmori, *Annu. Rev. Phys. Chem.* **60**, 487–511 (2009).
43. I. O. Antonov *et al.*, *Nat. Commun.* **12**, 2201 (2021).
44. P. Eberle *et al.*, *J. Phys. Conf. Ser.* **635**, 012012 (2015).
45. M. Hernández Vera *et al.*, *J. Chem. Phys.* **146**, 124310 (2017).
46. Y. Liu, Supplementary data for “Quantum state tracking and control of a single molecular ion in a thermal environment,” version 1, NIST Science Data Portal (2024); <https://doi.org/10.1126/science.ado1001>.

ACKNOWLEDGMENTS

We thank L. Liu and B. Margulis for careful reading of the manuscript. **Funding:** We acknowledge support from the US Army Research Office under grant W911NF-19-1-0172. **Author contributions:** Y.L., D.R.L., D.L., and C.-w.C. conceived of and designed the experiments. Y.L., Z.L., and C.-w.C. collected and analyzed the data. Y.L. and J.S. set up sources for 285- and 570-GHz microwaves. All authors provided suggestions for the experiments, discussed the results, and contributed to the editing of the manuscript. **Competing interests:** The authors declare that they have no competing financial interests. **Data and materials availability:** Data underlying various plots in this article are deposited in the National Institute of Standards and Technology (NIST) Science Data Portal (46). All other data needed to evaluate the conclusions in the paper are present in the paper or the supplementary materials. **License information:** Copyright © 2024 the authors, some rights reserved; exclusive licensee American Association for the Advancement of Science. No claim to original US government works. <https://www.science.org/about/science-licenses-journal-article-reuse>

SUPPLEMENTARY MATERIALS

science.org/doi/10.1126/science.ado1001
Materials and Methods
Supplementary Text
Figs. S1 to S4
Tables S1 to S3
References (47–50)

Submitted 22 January 2024; resubmitted 5 June 2024
Accepted 17 July 2024
Published online 1 August 2024
[10.1126/science.ado1001](https://doi.org/10.1126/science.ado1001)